RSC Advances

PAPER

View Article Online
View Journal | View Issue

Cite this: *RSC Adv.*, 2016, **6**, 62656

# A novel low-temperature solid-state route for nanostructured cubic garnet $Li_7La_3Zr_2O_{12}$ and its application to Li-ion battery

P. Jeevan Kumar,[ae] K. Nishimura,[b] M. Senna,*[ac] A. Düvel,[d] P. Heitjans,[d] T. Kawaguchi,[b] N. Sakamoto,[ab] N. Wakiya[ab] and H. Suzuki[ab]

We present a novel approach to the solid-state synthesis of garnet-type cubic $Li_7La_3Zr_2O_{12}$ (c-LLZO) nanostructured particles with 1.0 mass% Al at 750 °C within 3 h. In contrast to conventional solid-state processes, a highly reactive precursor was prepared in two steps: (i) by homogenizing the stoichiometric mixture without Li, and (ii) subsequent addition of Li in the form of an ethanolic solution of lithium acetate. The actual composition determined by ICP analysis was $Li_{6.61}La_3Zr_2Al_{0.13}O_{11.98}$. Sintering these nanoparticles at 1100 °C for 3 h in air after cold isostatic pressing brought a dense ceramic pellet with a relative density of 90.5%. The corresponding ionic conductivity with Au electrodes was $1.6 \times 10^{-4}$ S cm$^{-1}$ at room temperature. To study its electrochemical behavior as an electrolyte, a model cell of Li//(1 M $LiPF_6$ + c-LLZO)//$LiCoO_2$ configuration was constructed. Cyclic voltammetry of the cell delivered one set of redox couple with narrow voltage separation (15 mV) with a $Li^+$ diffusion coefficient at room temperature of about $2 \times 10^{-11}$ cm$^2$ s$^{-1}$ at the interface between $LiCoO_2$ and 1 M $LiPF_6$ + c-LLZO. The cell received an average discharge capacity of 64.4, 60.3, 56.1, 51.9 and 46.9 μA h cm$^{-2}$ μm$^{-1}$ at discharge rates 0.5C, 1C, 2C, 4C and 6C, respectively. The cell exhibited complete oxidation and reduction reactions with an average initial discharge capacity of about 64 μA h cm$^{-2}$ μm$^{-1}$, which is 92.7% of $LiCoO_2$ theoretical value. These observations indicate the applicability of the present c-LLZO as an electrolyte for a solid-state Li-ion battery.

Received 14th April 2016
Accepted 17th June 2016

DOI: 10.1039/c6ra09695f

www.rsc.org/advances

## Introduction

Lithium ion batteries (LIB) with higher safety and affordability are of utmost importance for better utilization of renewable energy and high-energy electric vehicles.[1,2] Stringent requirements are high-energy density, long cycle life with improved safety, reliability and leakage-free properties in wider operating temperature regimes, enabling a cost-effective process. In current battery technology, we have relatively promising electrode materials in terms of higher energy density and structural stability. On the other hand, we still use flammable, volatile and unstable organic solvents based electrolytes containing Li-salts with polymer separator in all types of conventional Li-ion batteries. These electrolytes not only cause irreversible capacity losses due to the formation of solid-electrolyte interphases (SEI), but also limit the safety of the batteries. Solid-state electrolytes (SSE) with fast Li-ion diffusion were recognized as promising alternative, addressing better thermal and chemical stabilities and opening a wider operational temperature window.[3] For the high-performance SSE, however, great challenges remain, such as: (i) increase in the ionic conductivity and (ii) optimization of fabrication processes.[4]

Within the variety of SSE including lithium superionic conductor (LISICON), thio-LISICON or sodium superionic conductor (NASICON), garnet-type c-LLZO is regarded as one of the most promising SSE due to its high ionic conductivity, stability with lithium and its less hygroscopic behavior.[5,6] Weppner and coworkers have succeeded first in synthesizing c-LLZO by sintering at 1230 °C for 36 h and obtained a total (bulk + grain boundary) ionic conductivity of $2.44 \times 10^{-4}$ S cm$^{-1}$ at 25 °C.[7] Thereafter, the material has received enormous research attention and a lot of work has been reported. LLZO garnet exhibits mainly two distinct phases, *i.e.* a tetragonal phase (t-LLZO) with low ion conductivity and a cubic phase with fast ion conductivity. The regulation of the Li site preference is found to be decisive for the phase purity of the cubic garnet structure and to yield fast ordered $Li^+$ kinetics. This has been managed by the addition of few mol% of Al, Ga, Ta, Fe, Nb *etc.*

---

[a] *Research Institute of Electronics, Shizuoka University, 432-8561, Hamamatsu, Japan*
[b] *Graduate School of Engineering, Shizuoka University, 432-8561, Hamamatsu, Japan*
[c] *Faculty of Science and Technology, Keio University, 223-8522, Yokohama, Japan. E-mail: senna@applc.keio.ac.jp*
[d] *Institute of Physical Chemistry and Electrochemistry, ZFM – Center for Solid State Chemistry and New Materials, Leibniz Universität Hannover, 30167, Hannover, Germany*
[e] *Centre for Nanomaterials and MEMS, Department of Physics, Nitte Meenakshi Institute of Technology (NMIT), Bangalore, 560064, India*

for substituting Li and probably also some of the other cation species in LLZO. The reason(s) for this is(are) still under investigation. Ohta *et al.* reported that substitution of Nb for Zr in LLZO not only hinders the Li-ion motion but also lowers the Li-ion content more than all other additives. They found an ionic conductivity as high as $8 \times 10^{-4}$ S cm$^{-1}$.[8] However, many reports suggested that Al or Ta is more preferable as compared to Nb from the viewpoint of chemical stability in the presence of Li.[9] Recently, Bernuy-Lopez *et al.* reported an ionic conductivity as high as 1.3 mS cm$^{-1}$ at room temperature (RT) by atmosphere controlled processing of Ga-doped LLZO.[10] However, as very recently shown by single crystal studies by Robben *et al.* and briefly after by Wagner *et al.* Ga-doping is accompanied by a reduction of the LLZO cubic garnet symmetry.[11,12] Buschmann *et al.* reported that Ga substituted LLZO/Li interface showed higher area specific interfacial resistance (ASR) (6000 Ω cm$^2$) than 0.9 wt% Al substituted LLZO/interface (2800 Ω cm$^2$).[13] Geiger *et al.* also suggested that a minor concentration of Al in LLZO (0.10 to 0.15 Al per formula unit) as stabilizing agent could compensate the additional charge emergence due to Li$^+$ vacancies and then reduce the free energy associated with ordering of the Li sub-lattice in LLZO core symmetry.[14]

Preparation of these oxide powders with complex garnet structure is mostly based on the conventional sol–gel or solid state syntheses, in which powders were calcined usually at temperatures above 850 °C. Xie *et al.*[15] and Kokal *et al.*[16] have succeeded in synthesizing phase pure c-LLZO nanopowders at lower temperatures of 750 °C, preceded by a solution and/or a sol–gel procedure. However, their product showed unfavorable ionic conductivities in the order of $\sim 10^{-6}$ S cm$^{-1}$ at room temperature (RT). Zhang *et al.* claimed higher ionic conductivity of $3.3 \times 10^{-4}$ S cm$^{-1}$ at RT for nano-sized Al-doped LLZO powders prepared *via* a novel wet-chemical method combined with post heating at 900 °C.[17] In an attempt to fabricate LIB with high capacity and reliability, Cheng *et al.* explored solid state synthesis of LLZO with controlled particle size.[18] By combining mechanochemical processing and subsequent heating, Düvel *et al.* succeeded in preparing quasi phase pure c-LLZO.[19] Table 1 exhibits the results reported on Al-substituted c-LLZO synthesized by conventional solid-state methods. Solid-state routes generally demand higher calcination temperatures and longer heating duration. Phase stability of c-LLZO is influenced by the Al and Li concentration, which are highly sensitive to prolonged heat treatment due to usage of $Al_2O_3$ crucibles and higher calcination temperatures, respectively.[20] Simultaneous formation of a pyrochlore phase often takes place, leading to the inferior ionic behavior of the ceramic. Based on those facts, our attempts were focused on the reduction of the calcination temperature and duration. Once c-LLZO powders are successfully prepared, it is often necessary to sinter them to obtain a dense pellet or a bulk ceramics for all-solid lithium ion battery.[21–23] Bulk sintered LLZO is also useful as a target for a physical vapor deposited thin film.[24] For the preparation of high-density sintered pellets, various additives were incorporated.[25] In order to increase the sinter density, using the starting mixture with smallest possible primary particles is another important viewpoint, since the associated high surface energy serves as an important driving force of sintering.[26–28]

In this paper, we report a novel methodology to synthesize phase pure c-LLZO nanostructured particles at lowest possible temperatures. For this purpose, we propose a two-step reaction scheme for the preparation of the precursor. In the first step, a precursor of La and Zr, with their electronegativity slightly higher as compared to that of Li is prepared under mechanical stress. Subsequently, a stoichiometric Li source is added as an ethanolic solution. In the latter process, lithium can penetrate further to its ordering into the sub-lattice sites in Zr octahedral and La tetrahedral environments of garnet structures. Fig. 1 schematically illustrates our concept of preparing c-LLZO in comparison to the conventional solid-state process. We further observed microstructural evolution of nanoparticles on cold isostatic pressing (CIP) followed by conventional sintering. After determining the Li-ion conductivities of the sintered pellet at different temperatures, a prototype of Li-ion battery has been crafted using thin c-LLZO sintered pellet as an electrolyte in combination with the two polymer separators soaked into

Table 1 Solid route syntheses of Al-substituted c-LLZO reported in literature

| Reference | Precursors | Calcination treatment | Relative density | Activation energy | Ionic conductivity (S cm$^{-1}$) at RT |
|---|---|---|---|---|---|
| Sakamoto *et al.*[39] | $LiCO_3$,$La(OH)_3$, $ZrO_2$, $Al_2O_3$, no excess Li | 1000 °C for 4 h | 98% | 0.26 eV | $4 \times 10^{-4}$ |
| Kotobuki *et al.*[22] | LiOH, $La(OH)_3$, $ZrO_2$, $Al_2O_3$ | 900 °C for 6 h | | | $2.4 \times 10^{-4}$ |
| Chen *et al.*[35] | $Li_2CO_3$, $La_2O_3$, $ZrO_2$, $Al_2O_3$, 10% excess Li | Two steps 900 and 1125 °C for 10 h each | 93% | | $2.48 \times 10^{-4}$ |
| Cheng *et al.*[18] | $Li_2CO_3$, $La(OH)_3$, $ZrO_2$, $Al_2O_3$, no excess Li | 1000 °C for 12 h | 94% | 0.29 eV | $2.3 \times 10^{-4}$ |
| Buschmann *et al.*[13] | LiOH, $La_2O_3$, $ZrO_2$, $Al_2O_3$, 10–20% excess Li | Calcination at 1130 °C for 12 h | | 0.34 eV | $4 \times 10^{-4}$ |
| Allen *et al.*[9] | $Li_2CO_3$, $La(OH)_3$, $ZrO_2$, $Al(OH)_3$, 3 wt% Li excess | 1000 °C for 3–4 h | 98% | 0.30 eV | $3.7 \times 10^{-4}$ |
| Lee *et al.*[23] | LiOH, $La_2O_3$, $ZrO_2$, 10 wt% excess Li | 900 °C for 12 h in alumina crucibles | 86% | 0.34 eV | $4.9 \times 10^{-4}$ |
| Present work | $CH_3COOLi$, $La(OH)_3$, $ZrO_2$, 1 wt% AlOOH, no excess Li | 750 °C for 3 h | 91% | 0.36(1) eV | $1.6 \times 10^{-4}$ |

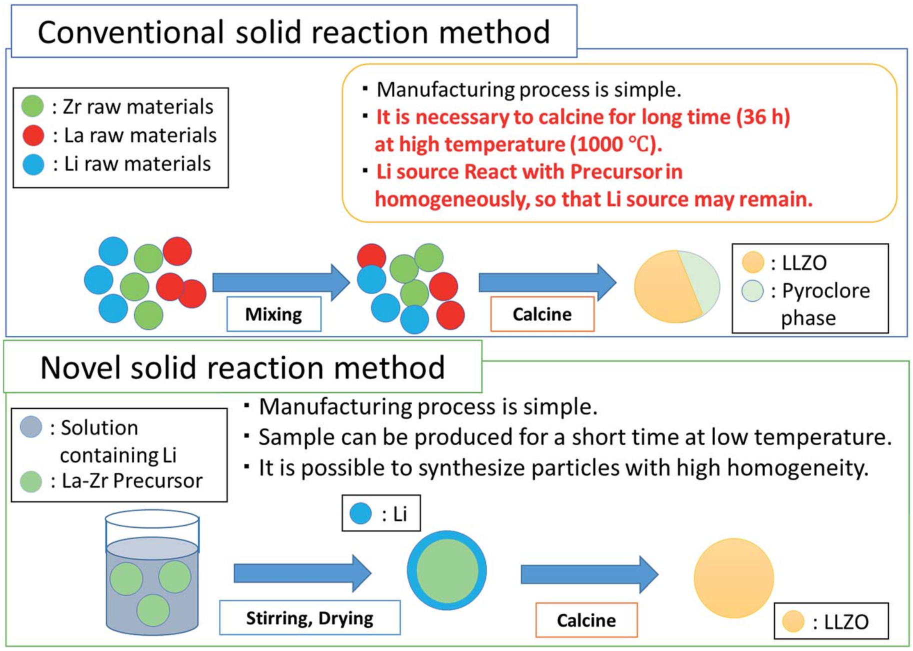

**Fig. 1** Conceptual representation of novel approach to solid state synthesis approach in contrast to conventional solid reaction method.

a non-aqueous electrolyte. Finally, the preliminary electrochemical performances were examined by using these prototypic LIB.

## Experimental section

### Sample preparation

LLZO precursor was prepared in two steps, *i.e.* from the precursors A and B. Precursor A was prepared from $ZrO_2$ nanoparticles (Tosoh ~99.9%, average particle diameter, $d_{avg.}$ = 270 nm) and $La(OH)_3$ (Aldrich 99.9%, $d_{avg.}$ = 190 nm) in a molar ratio 2 : 3. One mass% AlOOH (Wako ~97%, $d_{avg.}$ = 50 nm) was added for the stabilization of c-LLZO. They were mixed intimately in a planetary mill (Fritsch, Pulverisette 6) at 500 rotations per minute (RPM) for 3 h with 2 mm diameter $ZrO_2$ media in ethanol (EtOH) and carefully dried in air in 3 steps, *i.e.* 70 °C for 2 h, 100 °C for 0.5 h and 200 °C for 1 h. The precursor A was put into a 15 mass% ethanol solution of lithium acetate (Wako) and ultrasonicated for 10 min and dried under the same conditions to obtain precursor B with the exact stoichiometry of LLZO. The precursor B was calcined in air at 750 °C for 1–5 h. Powders were compressed by CIP at 60 MPa for 0.5 h. The green compact was subjected to sintering in a muffle furnace at 1100 °C for 3 h in air. Fig. 2 summarizes the novel solid-state reaction scheme adopted to synthesize c-LLZO.

### Characterization

Thermogravimetric/differential thermal analysis (TG-DTA) of the LLZO precursor powder was conducted by using a Thermo plus TG 8120 model spectrometer (Rigaku, Japan) under air atmosphere with $\alpha$-$Al_2O_3$ reference container. Crystal structures of the samples were examined using an X-ray diffractometer (D8 Advance; Bruker Analytik, Germany) equipped with a Cu anode ($\lambda = 1.5418$ Å) operated at 40 kV and 40 mA with a scanning rate in $2\theta$ of 0.01 $s^{-1}$. The phase composition was analyzed using TOPAS software utilizing the ICSD PDF database.

The external morphology of the powder samples calcined and the cross-sectional view of the pellet sintered were observed by field emission scanning electron microscopy (FESEM) (Model JSM-700F, JEOL Ltd., Tokyo, Japan) with an accelerating voltage of 15 kV. For the measurements the samples were prepared by attaching the powder/broken pellet to an aluminum stub with silver paste, which then was coated with osmium by sputtering to prevent surface charging. The microstructure of calcined LLZO samples was investigated using scanning transmission electron microscopy (STEM) (Model JEM-2100F; JEOL Ltd.) equipped with energy dispersive spectroscopy (EDS) operating at an accelerating voltage of 200 kV. For TEM evaluations powder samples were dispersed in ethanol using ultrasound for 10 min and one droplet was dropped on a carbon coated grid and dried overnight before analysis.

The particle size distribution of nanoparticles was measured in ethanol solvent using an electrophoretic scattering photometer, *i.e.* dynamic light scattering (DLS) (Photal SELS-800Y; Otsuka Electronics Co. Ltd. Tokyo, Japan). Inductively coupled plasma optical emission spectrometry (ICP-OES) studies were performed to determine the concentration of trace elements in synthesized LLZO powders by Optima 2100DV (PerkinElmer, USA).

Temperature-dependent impedance spectroscopy (IS) measurements were conducted at temperatures ranging from 273 K to 513 K. A broadband dielectric spectrometer (Novocontrol, Concept 41) was used for the measurements in the frequency range between $10^{-2}$ Hz and $10^{7}$ Hz with voltage ramp of 100 mV $s^{-1}$. Electrochemical tests of the cells were performed in Swagelok type cells using a thin slice of LLZO as electrolyte with lithium foil (area = 0.8 $cm^2$) negative electrode. RF

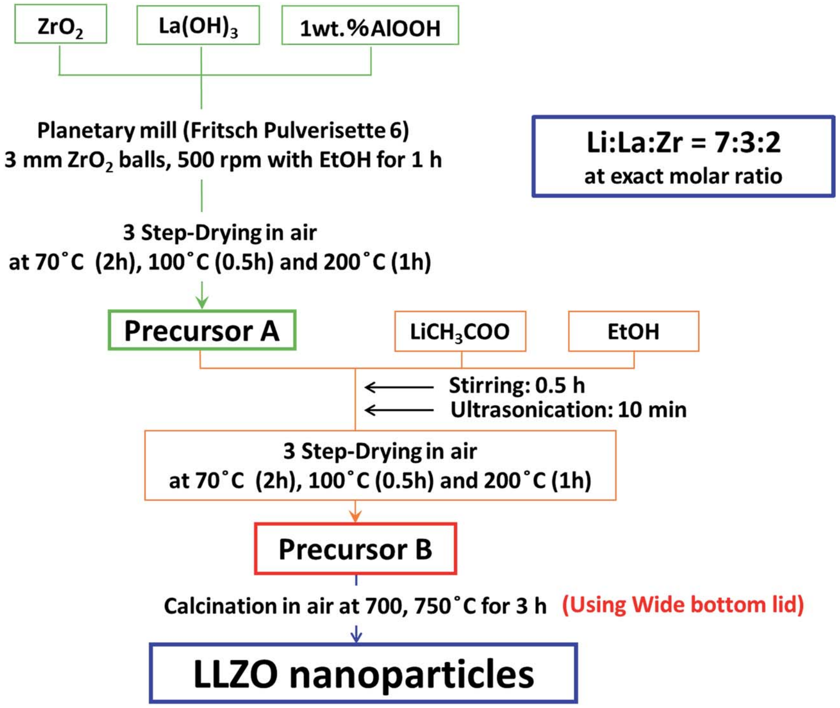

Fig. 2 Schematic diagram for the modified solid route synthesis of LLZO nanoparticles.

magnetron sputter deposited $LiCoO_2$ thin films on Pt/Si substrates have been used as working electrode. The active area of the working electrode was estimated to be 0.8 $cm^2$ and its thickness was 1.6 μm. Li-ion conductive polypropylene porous separators were introduced in between electrode(s) and LLZO electrolyte to minimize the unavoidable electrolyte-to-electrode(s) interfacial resistance. These polymer sheets were actually soaked in 1.0 M $LiPF_6$ in an ethylene carbonate (EC)–dimethyl carbonate (DMC) mixture (1 : 1 ratio by volume), overnight. The cell designed was annotated as Li//(1 M $LiPF_6$ + c-LLZO)//$LiCoO_2$ cell. All cells were assembled in an Ar-filled dry glove box ($O_2$, $H_2O$ below 5 ppm). The series of room temperature potentiostatic and galvanostatic electrochemical measurements such as cyclic voltammetry and chronopotentiometry were conducted with a Versastat 4 electrochemical analyzer (Tokyo corp., Japan) within the potential range 3.0–4.2 V and at various charge/discharge current rates.

## Results and discussions

### Properties of the precursors

The thermal behavior of the powder mixture, precursor A and precursor B is compared in Fig. 3A–C, respectively. The change in the DTA profiles due to mechanical stressing is significant, when we compare Fig. 3A and B. However, two endothermic peaks of the powder mixture, located at *ca.* 375 °C and 525 °C, which can be ascribed to the main decomposition of $La(OH)_3$ (ref. 29) and AlOOH,[30] survived after mechanical activation to prepare the precursor A. A sharp exothermic peak from precursor B, at around 390 °C, is attributed to the decomposition of lithium acetate with simultaneous burn-out of the decomposed product, mainly methane.[31] Two endothermic peaks observed in precursor A have disappeared in Fig. 3C in which the first endothermic peak *i.e.* around 375 °C appeared to be masked by the exothermic process. These features consistently indicate the significant chemical interaction between precursor A and Li acetate. Since the decomposition temperature of the lithium acetate did not exhibit big difference from its pure state, chemical interaction must have played a more significant role after its decomposition. As for the TG curves, the main weight loss at around 370–400 °C is much more significant for precursor B due to the overlapped decomposition of hydroxides and the acetate. However, the subsequent changes are fairly different, mainly due to the changes in the states of OH groups in the precursors. Details of these differences are, however, outside the scope of the present study.

### Crystallographic properties related to garnet phase purity

The conventional garnet structure has the general chemical formula of $A_3B_2(CO_4)_3$, where A, B and C reside at 8, 6 and 4 oxygen-coordinated sites, respectively. In a Li-stuffed garnet, *i.e.* in $Li_7La_3Zr_2O_{12}$, lithium occupies the B (L1) sites as well as unoccupied distorted octahedral (L2) sites. Fig. 4A and B compares the X-ray diffraction (XRD) patterns of LLZO precursor powders calcined at 700 and 750 °C for 3 h synthesized by our novel solid reaction method. It should be noted that these powders were synthesized at stoichiometric ratios of elements and no excess Li was added. The XRD results show that the cubic phase of LLZO was formed after calcining precursor B at 700 °C for 3 h. However, these powders exhibit additional reflections of impurity phases, *i.e.* $La_2Zr_2O_7$ (PDF 17-

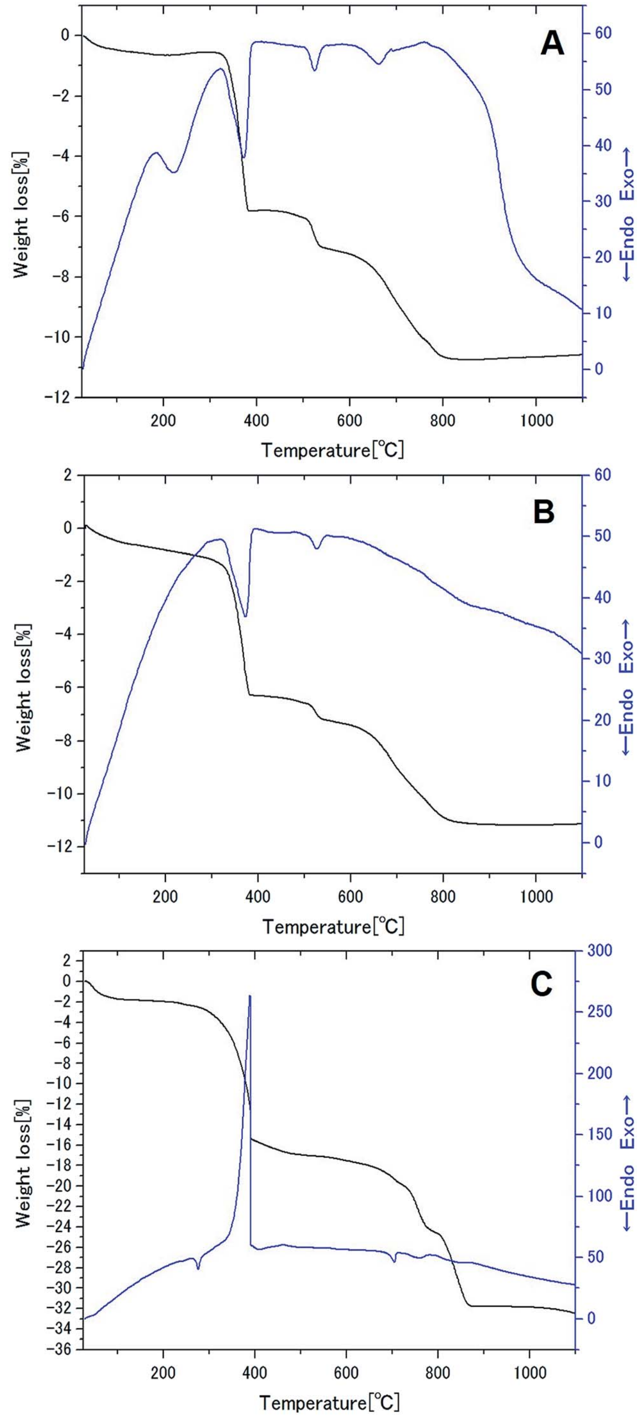

Fig. 3 TG-DTA profiles of (A) the powder mixture, (B) precursor A and (C) precursor B.

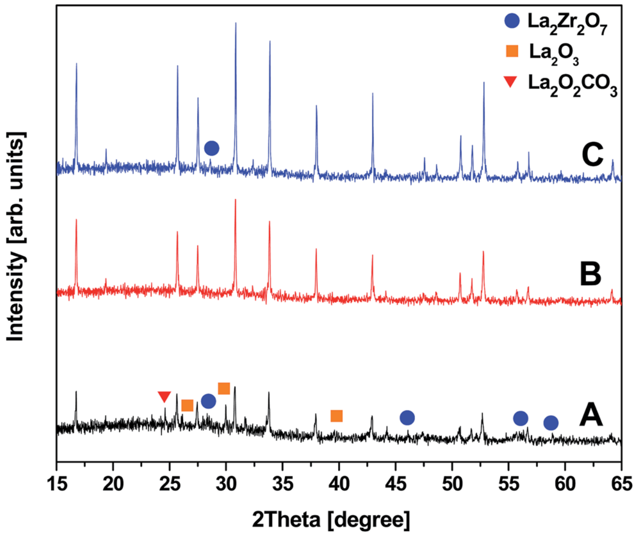

Fig. 4 (A and B) X-ray diffractograms of calcined LLZO nanoparticles calcined at 700 °C and 750 °C for 3 h, respectively, and (C) XRD plot of CIP sintered LLZO pellet, respectively ('●' denotes $La_2Zr_2O_7$, '■' denotes $La_2O_3$ and '▼' denotes $La_2O_2CO_3$ impurity peaks).

0450), $La_2O_3$ (05-0602) and $La_2O_2CO_3$ (PDF 37-0804), see Fig. 4A. By slightly increasing the calcination temperature to 750 °C while keeping the duration for 3 h, pure cubic phase LLZO is detected without any signature of impurities. The corresponding XRD pattern of cubic $Li_7La_3Zr_2O_{12}$ is shown in Fig. 4B. All the diffraction peaks can be matched with a typical cubic garnet phase similar to $Li_5La_2Nb_2O_{12}$ (PDF 01-084-1753), and no obvious impurity phases can be detected. The lattice parameter $a = 12.97093$ Å was calculated by profile fitting of the powder XRD pattern using Topas program. It is in good agreement with published results.[32] The crystallite size estimated from the FWHM of the X-ray diffractometry was about 135.8 nm. These observations agree with those from TG-DTA. The high garnet phase purity in LLZO powders at low calcination temperatures is achieved in a relatively short period of time. This could be attributed to the reaction of the Li precursor in liquid form with the mechanically activated, highly reactive LaZr precursor and the addition of Al as dopant. Zhang *et al.* demonstrated the importance of addition of $Al_2O_3$ to crystallize the cubic phase of LLZO, however, at higher calcination temperature and prolonged heating time (900 °C, for about 4 h).[33] As reported by Hubaud *et al.* $Al^{3+}$ was incorporated at the grain boundary by forming $Li_5AlO_4$ at lower temperature. It entered into the grain by reaction with the tetragonal phase to form cubic phase LLZO when sintered at high temperature.[34] According to literature, $Al^{3+}$ most probably substitutes $3Li^+$ and stabilizes the cubic phase rather than the tetragonal phase, which is stable at room temperature (without $Al^{3+}$).[35] These XRD patterns were compared with that of an LLZO pellet prepared by CIP and sintering at a temperature of 1100 °C for 3 h. The sintered pellet also exhibited a diffraction pattern similar to its powders and demonstrated cubic garnet structure, as shown in Fig. 4C. Although a very small amount of $La_2Zr_2O_7$ was detected, it is clear that the phase purity of c-LLZO was almost maintained after sintering the compressed calcined powders. The existence of minute pyrochlore signature is probably due to a partial diffusion of Li-ions out of the green pellet while sintering. We also noted an increase in the XRD peak intensities for the sintered sample, showing the increase in the crystallinity of the LLZO. The crystallite size and the lattice parameter $a$ obtained after Rietveld refinement were about 145.2 nm and 12.9770 Å, respectively. Estimated lattice parameters are in agreement with the literature.[32]

To understand the phase purity of the calcined LLZO polycrystalline powders (750 °C for 3 h) and the corresponding sintered LLZO pellet, unpolarized micro-Raman spectroscopic studies were conducted in the wavenumber range from 100 to 550 $cm^{-1}$. The results are plotted in Fig. 5A and B, respectively. In general, t-LLZO exhibits more complicated spectral features than the cubic phase either due to the lower symmetry of the tetragonal garnet ($I4_1/acd$ space group) or due to more disordered $Li^+$ ion arrangements, as summarized by Tietz *et al.*[36] According to Orera *et al.*,[37] Raman modes confined to the region between 330 and 600 $cm^{-1}$ might be particularly sensitive to the Li-ion distributions and its changes in the symmetry. The Raman signals visible in the low frequency region, *i.e.* <150 $cm^{-1}$, are mainly of La based vibrational bands. Fig. 5A and B clearly exhibit overall similarities in Raman excitations at wave numbers around 107, 121, 144, 209, 251, 361, 410 and 514 $cm^{-1}$ for both, calcined and sintered, LLZO powders. No splitting of Raman bands was observed in the low-frequency region, *i.e.*, at wavenumbers 107 ($T_{2g}$) and 121 ($E_g$) $cm^{-1}$ nor in $Li^+$ ion bonding sensitive regions, *i.e.* at 361 ($T_{2g}$), 410 ($E_g/T_{2g}$) and 514 ($T_{2g}/E_g$) $cm^{-1}$, respectively. These observations indicate the phase purity of both the samples ascribed to the characteristic cubic garnet structure with $I\bar{4}3d$ space group. Again, these observations were in good agreement with the ones reported in the literature.[37] It is also noticed that the Raman spectrum of calcined LLZO precursor powder exhibited additional spectral features with minute Raman intensities at wavenumbers 155 and 190 $cm^{-1}$ (Fig. 5A). These Raman signals were ascribed to the $T_{2g}$ and $E_g$ symmetries of t-LLZO garnet structure which later disappeared after sintering the CIP pressed LLZO powders (Fig. 5B) at elevated temperature (1100 °C for 3 h). A slight blue shift in all Raman excitations was observed for the sintered pellet which may be due to the development of strain in the confined grain growth. Structural rearrangement might have built up for the tiny inhomogeneous calcined precursor powders upon thermal treatment. The presence of additional phase was not reflected in the XRD observations due to its low sensitivity to the light weight elements. However, Raman scattering measurements could be able to clearly distinguish the presence of various phases in LLZO that are difficult to detect by XRD since they are present in very small concentrations.

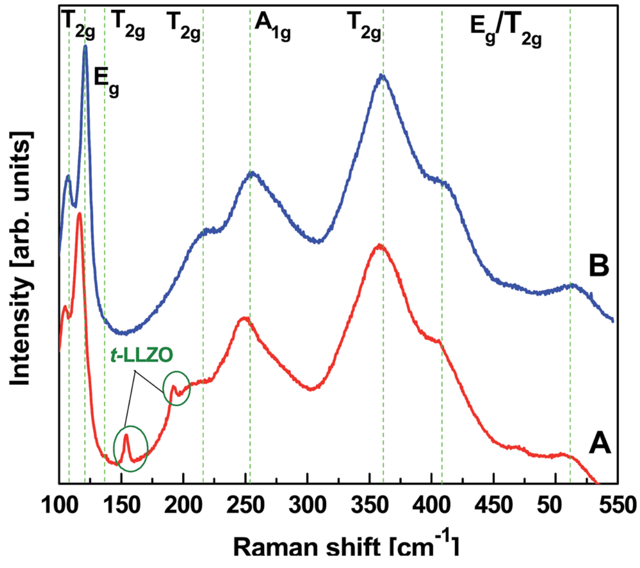

Fig. 5 Unpolarized micro-Raman spectra obtained from polycrystalline LLZO (A) after calcining the precursor B at 750 °C for 3 h and (B) the sintered LLZO pellet at 1100 °C for 3 h.

Fig. 6A and B show SEM images of the calcined LLZO powders at different magnifications. Fig. 6C shows the corresponding particle size distribution obtained from the DLS spectrum. In Fig. 6A and B, we observe the irregular block with the typical particle size distribution of 1–2 µm. At the same time, we recognize much smaller particulate units densely agglomerated. On the other hand, DLS measurements from the supernatant gave rise to an average size of *ca.* 90 nm. The average crystallite size estimated from the X-ray diffraction peak width was around 145 nm. This altogether gave us consistent information that our as-calcined LLZO powders have a primary particle size in the order of about 100 nm, are, however, agglomerated to particle sizes in the order of 1 to 2 µm. As shown in Fig. 6D, the particle sizes after sintering remain practically unchanged from those of agglomerated as-calcined powders, indicating that the sintering took place preferentially within the agglomerates.

The pellet density was estimated by weighing the pellets' mass and measuring their diameter and height. It is about 4.606 g $cm^{-3}$ which is about 90.5% of c-LLZO theoretical density (5.098 g $cm^{-3}$).[32] For comparison, the relative density of the pellet was also examined by the conventional Archimedes method and is almost identical to the projected value. Morphological features at fractured surface of the sintered pellet are shown in Fig. 6D. From the figure it is clear, that there are residual pores between and in the crystallites. However, the sample seems to be quite dense and is in agreement with the calculated high relative density without significant voids. The fracture of the pellet appears to be transgranular, indicating the grain boundary strengthening effect. All the ceramic grains exhibited irregular disc shaped morphology with an average grain size estimated to be around 4 µm.

Fig. 7A–E presents the STEM images of the as-calcined LLZO powders and corresponding EDS elemental mapping. Results indicate a fairly homogeneous distribution of La, Zr, and Al. The actual cationic concentration for the powders synthesized estimated by ICP was $Li_{6.61}La_3Zr_2Al_{0.13}O_{11.98}$, where the oxygen concentration was calculated to maintain charge neutrality. These observations consistently support the XRD and Raman results, demonstrating the cubic phase purity of the calcined powders.

## Impedance spectra of sintered pellet

Temperature and frequency dependences of the conductivity for the sintered pellet with blocking electrodes are displayed in Fig. 8. At each temperature, the conductivity spectra show dispersion regions, at higher and lower frequencies. The lower

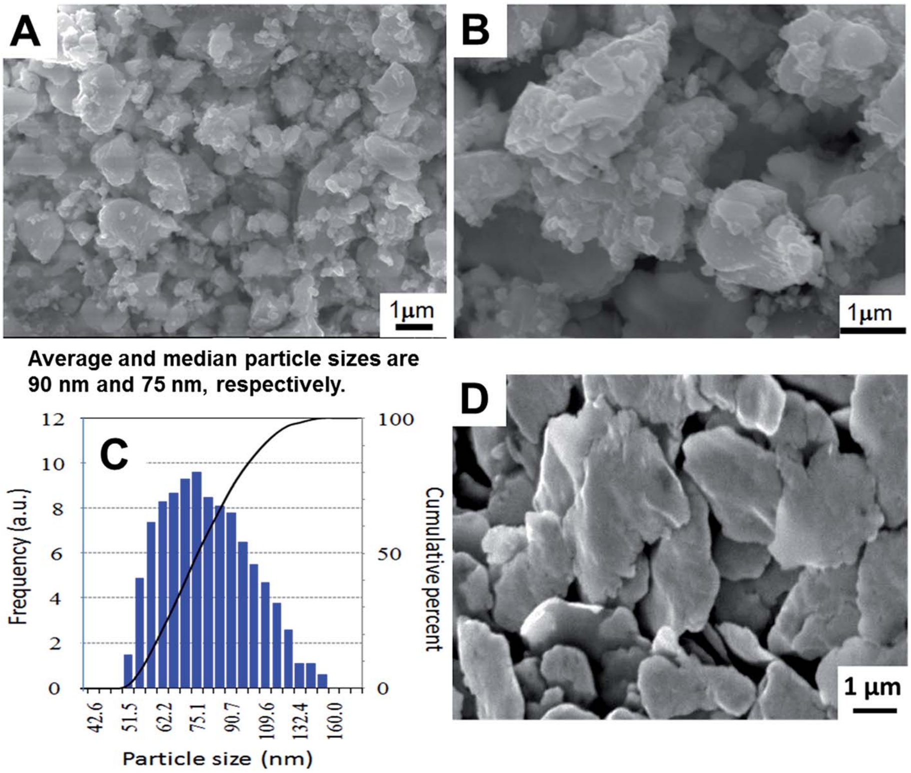

Fig. 6 (A and B) Scanning electron micrographs of the calcined LLZO nano particles at different magnifications, (C) particle size distribution of calcined LLZO demonstrated by DLS was displayed and (D) the cross-sectional view of sintered LLZO pellet.

ionic conductivity values in the lower frequency region indicate the presence of electrode polarization. Apparent plateau regions of the ionic conductivity were observed at the higher frequency side (between $10^3$ and $10^7$ Hz). These plateaus are observed to be shifted to smaller frequencies side with decreasing temperature. This signature indicates the single phase crystalline ceramic response upon the influence of frequency variation suggested by Jonscher *et al.*[38] Each plot consists of a frequency independent plateau region at higher and lower frequencies probably corresponding to the bulk ion conductivity ($\sigma_{\rm hf}$) and the grain boundary conductivity ($\sigma_{\rm lf}$), respectively. The temperature dependence of the conductivity is described by the Arrhenius relation:

$$\sigma T = A\mathrm{e}^{(-E_\mathrm{a}/k_\mathrm{B}T)} \tag{1}$$

here, $A$ is the pre-exponential factor, $E_\mathrm{a}$ is the activation energy for ionic conduction, and $k_\mathrm{B}$ is the Boltzmann constant.

Typical complex impedance plots for LLZO at various temperatures ranging from 293 K to 513 K are presented in Fig. 9, in Nyquist representation. In both the cases, the experimental complex impedance plot consists of a depressed semicircle accompanied by a straight line on the low frequency side which is suggestive of electrolyte–electrode polarization at the Au blocking electrodes. The depression of the semicircle may be ascribed to the presence of distribution in relaxation times within the bulk response. Again, the radius of the depressed semicircle is observed to decrease with increasing temperature due to the increase in the conductivity of the sample. The equivalent circuit (physical model) appropriate to these plots is shown in the inset of Fig. 9. The impedance data at all the temperatures can also be fitted with the above equivalent circuit. The equivalent circuit consists of a $\mathrm{CPE_2}$, acting as a blocking double layer capacitance in series with the parallel combination of bulk resistance ($R_2$) and constant phase element ($\mathrm{CPE_1}$), where CPE is generally considered as a leaky capacitor (*i.e.* hybrid between a resistor and a capacitor). Ideally the impedance assembly related to the process of charge transport in the bulk specimen is represented by parallel combination of $R_\mathrm{b}$ and $C_\mathrm{b}$,[8] where $R_\mathrm{b}$ represents the bulk resistance and capacitance $C_\mathrm{b}$ arises due to the electric relaxation process. But in this case we have replaced $C_\mathrm{b}$ with $\mathrm{CPE_1}$, which accounts for the observed depression of the semicircle and also the non-ideal electrolyte symmetry.[9] $\mathrm{CPE_2}$ in the equivalent circuit accounts for the formation of the inclined straight line in the low frequency region. The ion conductivity at each temperature was obtained by using the relation

$$\sigma = \frac{l}{Z_\mathrm{re}A} \tag{2}$$

here, $Z_\mathrm{re}$ which has been considered as $R_2$ is the bulk resistance of the sample. $Z_\mathrm{re}$ at each temperature was obtained from the intercept of the semicircle with the real axis. $l$ is the thickness and $A$ is the area of the plane parallel sides of the sample. From the intercept with the $Z_\mathrm{re}$ axis and the sample size, we estimated the specific conductivity of the present sintered body to be $1.6 \times 10^{-4}$ S cm$^{-1}$ at 293 K being comparable with previous results (Table 1).

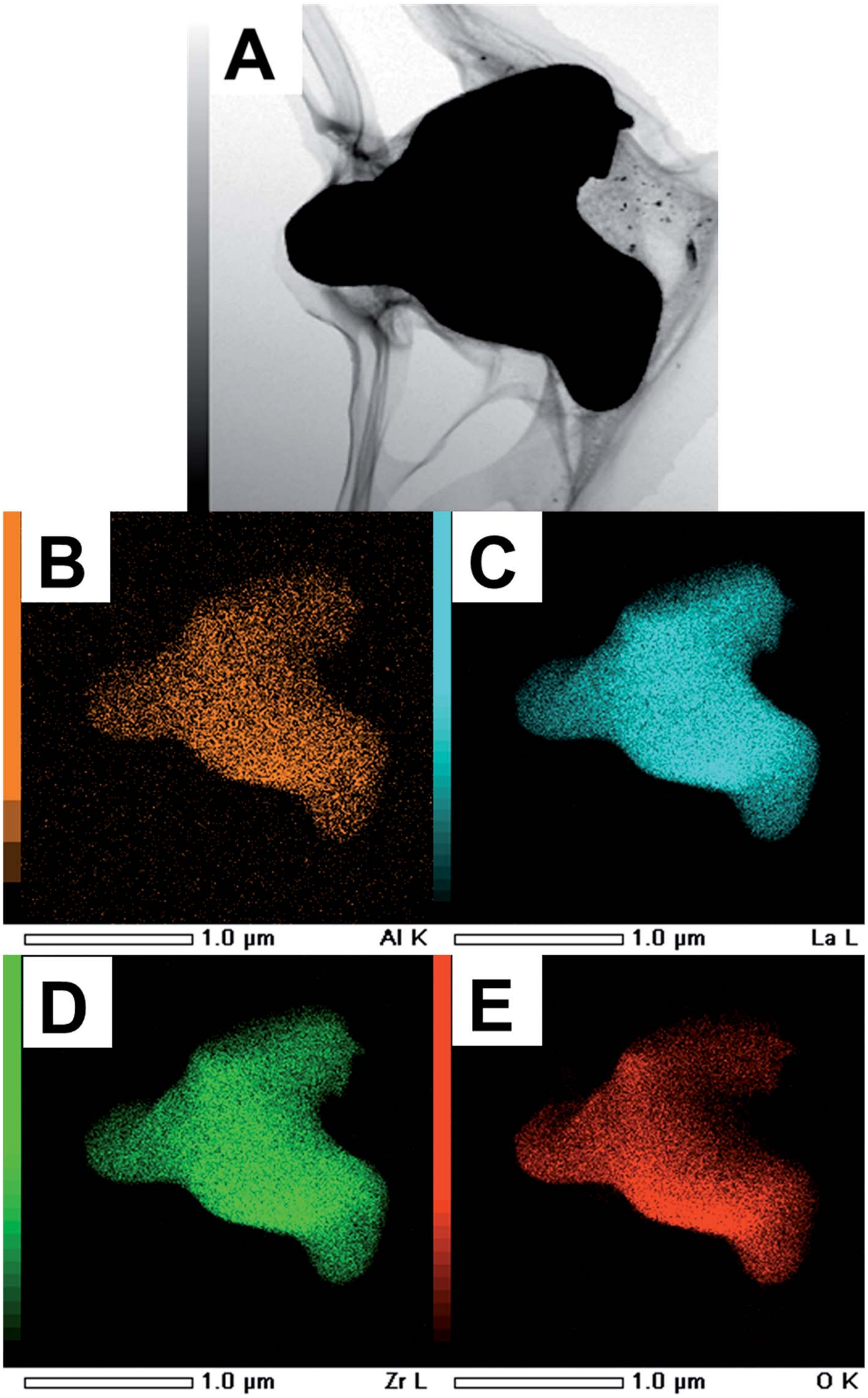

Fig. 7 (A) STEM images of the LLZO calcined powders and (B–E) area distribution of elements of Al, La, O and Zr measured by EDS, respectively.

Sakamoto *et al.*[39] showed higher total ionic conductivity values (4 × $10^{-4}$ S $cm^{-1}$) for c-LLZO containing only Al, however, with prolonged heating at higher calcination temperatures (>850 °C). From Table 1 it is clear that either excess amounts of Li or prolonged heating time should assist the synthesis for obtaining phase pure c-LLZO.[39] We present the conceivable ionic conductivity of the sintered pellet derived from c-LLZO nano precursor powders, calcined at notable reduced temperatures and time without adding excess Li ($Li_{6.61}La_3Zr_2Al_{0.13}O_{11.98}$). Fig. 10 shows the temperature dependence of the total ionic conductivity ($\sigma$) evaluated from the impedance plots of Fig. 9 based on the Arrhenius representation. Activation energy ($E_a$) was determined from the slope of the log($\sigma T$) *versus* 1000/$T$ plot. The calculated $E_a$ is 0.34 eV in the temperature range 233–400 K. This activation

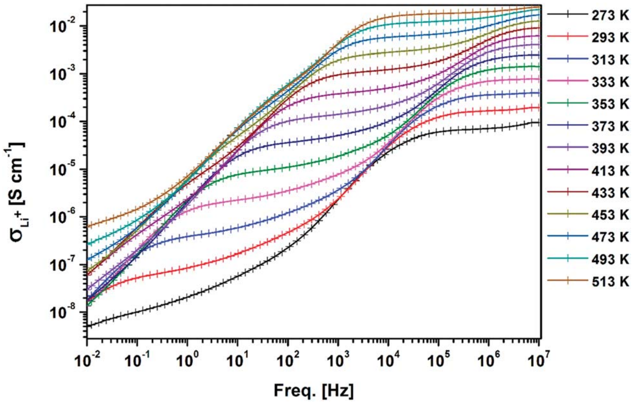

Fig. 8 AC conductivity of the sintered LLZO with Au blocking electrodes with respect to frequency at different temperatures.

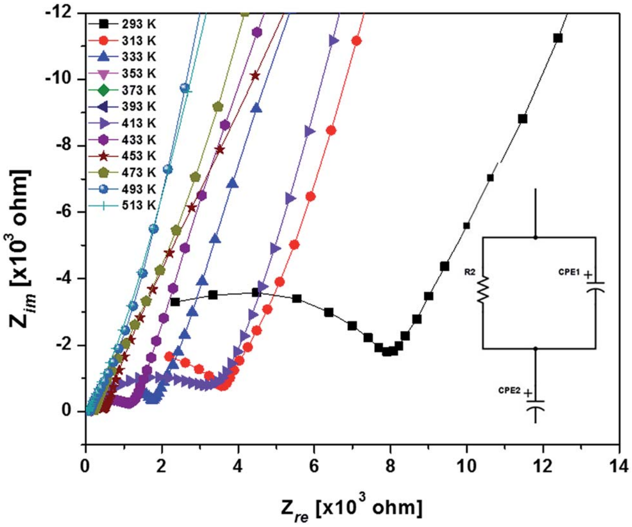

Fig. 9 Nyquist plots of the sintered LLZO with Au blocking electrodes around room temperature (inset: the equivalent circuit *i.e.* physical model appropriate to Nyquist plots).

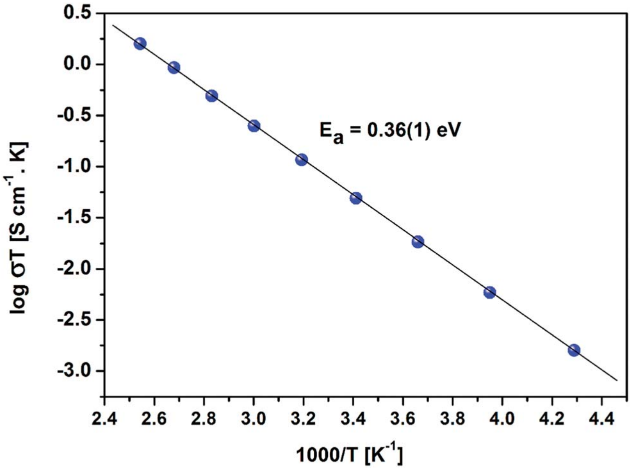

Fig. 10 Arrhenius plot of the sintered LLZO with Au blocking electrodes.

energy value is about 10% higher than the value determined by Murugan *et al.*[7] of 0.30 eV and about 10% lower than the value determined by Shimonishi *et al.*[40] of 0.37 eV. The reasons behind the difference of the reported activation energies are still unclear.[41] It may be associated, at least partly, with the lithium loss at the grain boundaries. Lower lithium loss should result in higher conductivity of grain boundaries as suggested by Ban and lead to a lower activation energy.[42] A comparison of properties derived from cubic LLZO fabricated by our approach to solid state synthesis with the reported ones are listed in Table 1. Note that the present novel strategy reduced the calcination temperature by about 250–350 °C as compared the conventional solid-state methods.

## Electrochemical properties of LLZO solid electrolyte based cell

Electrochemical measurements were carried out using a thin pellet of c-LLZO (0.15 mm thin, 0.608 cm$^2$ area) by designing a novel hybrid Li//(1 M $LiPF_6$ + c-LLZO)//$LiCoO_2$ cell. Schematic representation of the cell is shown in Fig. 11. We report a novel strategy to investigate electrochemical performance of the Li-ion cell using solid electrolyte in combination with conventional organic electrolytes. Using electrolyte soaked paper in between electrode and electrolyte, greatly reduces the electrode/electrolyte interfacial resistance. The concept of this novel cell structure was established from the work presented by Liu *et al.* on Li–$H_2O_2$ semi fuel cell.[43] A similar strategy was adopted by Kumazaki *et al.* who reported lithium plating stripping reaction at the Pt/LLZO pellet.[44] Analogous to these reports, we have used conventional polypropylene separator soaked in 1 M $LiPF_6$ with 1 : 1 EC : DMC, as $Li^+$ conducting media between LLZO pellet and cathode/anode. This is to reduce the electrode/LLZO electrolyte interfacial resistance. RF magnetron sputter deposited $LiCoO_2$ thin films coated on Pt/Si substrate has been used as positive electrode.

The galvanostatic and potentiostatic measurements on the cell are displayed in Fig. 12A and B, respectively. A cyclic voltammogram of cell measured in the cut-off potentials range from 4.2 to 3.0 V with a slow scan rate of 0.05 mV s$^{-1}$ is shown in Fig. 12A. The cell exhibited completely reversible electrochemical reactions with one set of redox peak currents located at 3.898/3.913 V with a potential separation of 15 mV *vs.* Li/$Li^+$ reference electrode. The higher current densities at redox peak potentials with complete reversibility indicate the signature of reduced IR drop and faster $Li^+$ kinetics of the hybrid cell designed with the combination of organic and crystalline electrolyte. These results are well congruent with the previous results reported on the Li//$LiCoO_2$ cell constructed with conventional organic electrolyte.[45] Like the results reported on Li//$LiCoO_2$ organic cell, two sets of tiny shoulder like redox couples were 4.081/4.077 V and 4.174/4.163 V (labeled in Fig. 12A as dashed lines I, II) corresponding to a phase transition of positive electrode.[46] As can be seen, besides higher ionic conductive LLZO solid electrolyte, the conventional organic electrolyte separator sheet had a lower cathodic/anodic

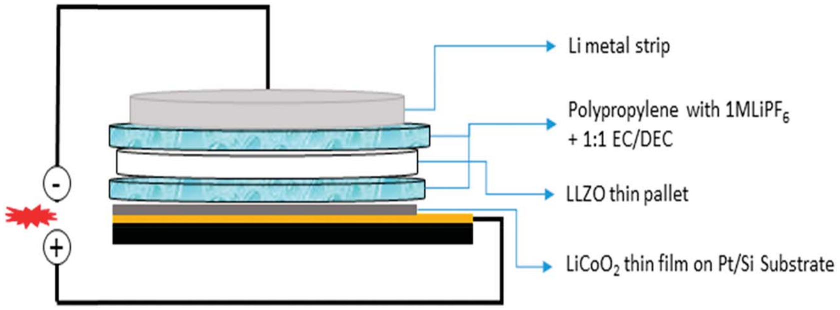

Fig. 11 Schematic diagram of the hybrid electrochemical cell constructed in Li//(1 M $LiPF_6$ + LLZO)//$LiCoO_2$ configuration.

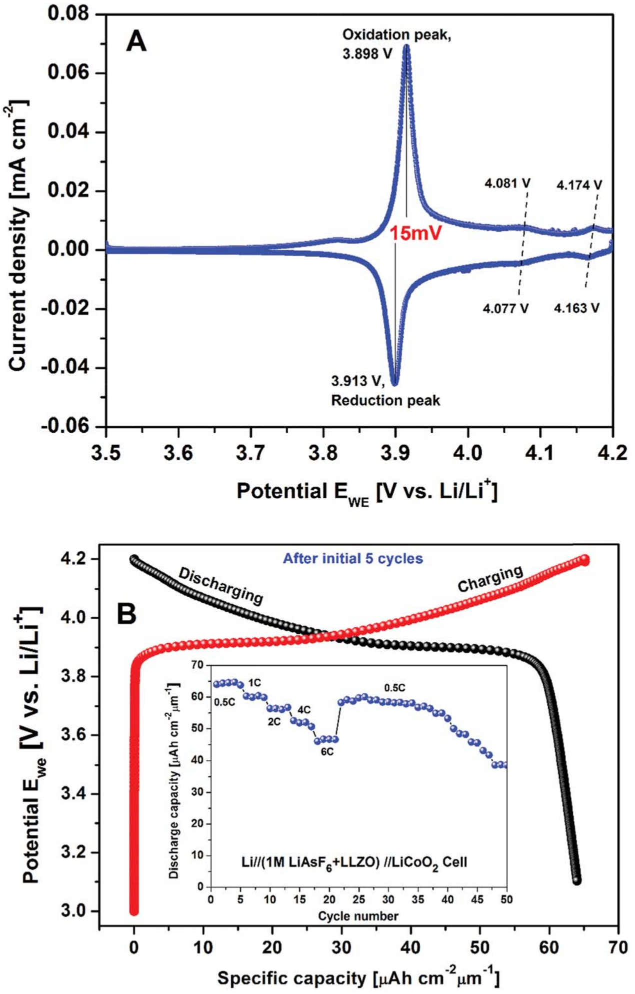

Fig. 12 Electrochemical performance of the Li//(1 M $LiPF_6$ + LLZO)//$LiCoO_2$ cell; (A) CV plot of the cell at scan rate 0.05 mV $s^{-1}$ between potential window 3.0–4.2 V and (B) initial charge/discharge capacities of the cell (after first 5 cycles) (inset: C-rate performance including cycleability of the cell).

interfacial resistance in the cell as well. Lower resistance of the hybrid combination of LLZO + organic electrolyte structure resulted in higher performance of the lithium cell. From the CV plot (Fig. 12A), the average $Li^+$ ion diffusion co-efficient in the electrochemical reaction can be obtained by the following equation[47]

$$I_p = 2.69 \times 10^5 A n^{3/2} C_o D_L{}^{1/2} \upsilon^{1/2} \tag{3}$$

here, $I_p$ is the peak current, $A$ is the surface area of the cathode, $n$ is stoichiometric number of electrons involved in the reaction, $C_o$ is the $Li^+$ concentration in the electrode, $D_L$ is the diffusion co-efficient of lithium ions and $\upsilon$ is the scan rate. Using eqn (3), the chemical ($Li^+$) diffusion coefficient at electrode/electrolyte *i.e.* $LiCoO_2$//(1 M $LiPF_6$ + c-LLZO) interface was calculated to be about $1.95 \times 10^{-11}$ $cm^2$ $s^{-1}$ at RT. This value is in close agreement with the data reported on the organic electrolyte based Li//$LiCoO_2$ cell.

The potential–capacity relationship after 5 cycles is shown in Fig. 12B. Its inset presents the C-rate performance of the hybrid cell discharged for about 50 cycles after initial 5 cycles. At the end of each cycle, a study time of 1 h was maintained. Thus, it is evident that the hybrid combination of the cell exhibits the best rate performance with an average discharge capacity of 64.4, 60.3, 56.1, 51.9 and 46.9 μA h $cm^{-2}$ $\mu m^{-1}$ at 0.5C, 1C, 2C, 4C and 6C, respectively. Even after, the cell performance was observed to be consistent, when the cell was continued to run at 0.5C rate and delivered an average discharge capacity of 64.4 μA h $cm^{-2}$ $\mu m^{-1}$ (~128 mA h $g^{-1}$). This value is about 92.7% of the theoretical capacity of $LiCoO_2$.[45] These observations are consistent with the work reported by Iriyama *et al.* on c-LLZO/$LiCoO_2$ interface modification with thin layer of Nb.[48]

Thus, the present c-LLZO based prototypic LIB exhibits fairly higher discharge capacity with higher coulombic efficiency with the hybrid combination of liquid and solid interface. These encouraging results are probably due to the combination of crystalline/organic electrolyte which derived the enhanced electronic conductivity. These observations are in good agreement with the CV measurements *i.e.* voltage plateaus observed in charge discharge curves are well matched with redox peak potentials observed from the CV curve.

A fairly large capacity fade (~0.5 μA h $cm^{-2}$ $\mu m^{-1}$ per cycle) as compared to the cell designed with organic electrolytes after 50 cycles (0.12 μA h $cm^{-2}$ $\mu m^{-1}$ per cycle)[49] remains as a week point of our prototypic LIB. We actually observed some traces of $LiCoO_2$ cathode peel off, after the electrochemical measurements. Development of an all solid state LIB, now being in progress in our group will be an option to solve the problem.

## Conclusions

In this study, we demonstrated a novel strategy to synthesize phase pure garnet structured LLZO with the formula $Li_{6.61}La_3Zr_2Al_{0.13}O_{11.98}$ *via* a solid state route by calcining at 750 °C for 3 h in air. The average primary particle size was at around 100 nm, as consistently evaluated from electron micrograph, dynamic light scattering and XRD. This was achieved by starting from the highly reactive precursor prepared by a two-step mechanochemical process. By sintering at 1100 °C for 3 h in air after CIP brought about the relative density of 90.5%. The ionic conductivity of the sintered pellet in Au//c-LLZO//Au structure was examined at different temperatures ranging from 273 to 513 K at atmospheric pressure and observed to be in the order of $1.6 \times 10^{-4}$ S cm$^{-1}$ at 293 K. To elucidate its practical application as an electrolyte, we designed a hybrid cell with Li//(1 M $LiPF_6$ + c-LLZO)//$LiCoO_2$ configuration with a thin sheet of sintered c-LLZO pellet as $Li^+$ conducting media and studied the electrochemical properties. The cyclic voltammogram of the cell exhibited a single set of redox couple with 15 mV of narrow voltage separation with a $Li^+$ diffusion coefficient at RT of about $1.95 \times 10^{-11}$ cm$^2$ s$^{-1}$ at electrode/electrolyte *i.e.* $LiCoO_2$//(1 M $LiPF_6$ + c-LLZO) interface. The cell reached an average discharge capacity of 64.4 μA h cm$^{-2}$ μm$^{-1}$ in the first cycle, which is 92.7% of theoretical value of the cathode. Again, the electrochemical activity of the cell was examined at various discharge rates *i.e.* 0.5C, 1C, 2C, 4C and 6C. By comparison, this novel solid state reaction method shows great advantages for synthesizing phase pure c-LLZO material including lower calcination temperature and less heat treatment process than other reported methods. The present work provides a new and very promising method for the preparation of high-performance LLZO solid electrolytes for the development of all solid state lithium ion battery.

## Acknowledgements

This work was supported by V4-Japan Joint Research Program, Structure – function relationship of advanced nano-oxides for energy storage devices (AdOX) granted from Japan Science and Technology Agency. Partial support was also obtained from the Deutsche Forschungsgemeinschaft (DFG) Research Unit 1277 (molife) and the Ministry for Science and Culture (MWK) of the Federal State of Lower Saxony, Germany. Open Access was financed by Leibniz Universität Hannover, Germany.

## References

1 C. Cao, Z. B. Li, X. L. Wang, X.-B. Zhao and W.-Q. Han, *Frontiers in Energy Research*, 2014, vol. 2.
2 B. Scrosati and J. Garche, *J. Power Sources*, 2010, **195**, 2419–2430.
3 P. Verma, P. Maire and P. Novák, *Electrochim. Acta*, 2010, **55**, 6332–6341.
4 B. S. Joo Gon Kim, S. Mukherjee, N. Schuppert, A. Bates, O. Kwon, M. J. Choi, H. Y. Chung and S. Park, *J. Power Sources*, 2015, **282**, 299–322.
5 V. Thangadurai, S. Narayanan and D. Pinzaru, *Chem. Soc. Rev.*, 2014, **43**, 4714–4727.
6 J. B. Goodenough and P. Singh, *J. Electrochem. Soc.*, 2015, **162**, A2387–A2392.
7 R. Murugan, V. Thangadurai and W. Weppner, *Angew. Chem., Int. Ed.*, 2007, **46**, 7778–7781.
8 S. Ohta, T. Kobayashi, J. Seki and T. Asaoka, *J. Power Sources*, 2012, **202**, 332–335.
9 J. L. Allen, J. Wolfenstine, E. Rangasamy and J. Sakamoto, *J. Power Sources*, 2012, **206**, 315–319.
10 C. Bernuy-Lopez, W. Manalastas, J. M. Lopez del Amo, A. Aguadero, F. Aguesse and J. A. Kilner, *Chem. Mater.*, 2014, **26**, 3610–3617.
11 L. Robben, E. Merzlyakova, P. Heitjansb and T. M. Gesing, *Acta Crystallogr., Sect. E: Crystallogr. Commun.*, 2016, **72**, 287–289.
12 R. Wagner, G. J. Redhammer, D. Rettenwander, A. Senyshyn, W. Schmidt, M. Wilkening and G. Amthauer, *Chem. Mater.*, 2016, **28**, 1861–1871.
13 H. Buschmann, J. Dolle, S. Berendts, A. Kuhn, P. Bottke, M. Wilkening, P. Heitjans, A. Senyshyn, H. Ehrenberg, A. Lotnyk, V. Duppel, L. Kienle and J. Janek, *Phys. Chem. Chem. Phys.*, 2011, **13**, 19378–19392.
14 C. A. Geiger, E. Alekseev, B. Lazic, M. Fisch, T. Armbruster, R. Langner, M. Fechtelkord, N. Kim, T. Pettke and W. Weppner, *Inorg. Chem.*, 2011, **50**, 1089–1097.
15 H. Xie, Y. Li and J. B. Goodenough, *Mater. Res. Bull.*, 2012, **47**, 1229–1232.
16 I. Kokal, M. Somer, P. H. L. Notten and H. T. Hintzen, *Solid State Ionics*, 2011, **185**, 42–46.
17 Y. Zhang, J. Cai, F. Chen, R. Tu, Q. Shen, X. Zhang and L. Zhang, *J. Alloys Compd.*, 2015, **644**, 793–798.
18 L. Cheng, J. S. Park, H. Hou, V. Zorba, G. Chen, T. Richardson, J. Cabana, R. Russo and M. Doeff, *J. Mater. Chem. A*, 2014, **2**, 172–181.
19 A. Düvel, A. Kuhn, L. Robben, M. Wilkening and P. Heitjans, *J. Phys. Chem. C*, 2012, **116**, 15192–15202.
20 E. Rangasamy, J. Wolfenstine, J. Allen and J. Sakamoto, *J. Power Sources*, 2013, **230**, 261–266.
21 S. W. Baek, J. M. Lee, T. Y. Kim, M. S. Song and Y. Park, *J. Power Sources*, 2014, **249**, 197–206.
22 M. Kotobuki, K. Kanamura, Y. Sato and T. Yoshida, *J. Power Sources*, 2011, **196**, 7750–7754.
23 J. M. Lee, T. Kim, S. W. Baek, Y. Aihara, Y. Park, Y. I. Kim and S. G. Doo, *Solid State Ionics*, 2014, **258**, 13–17.
24 J. Tan and A. Tiwari, *ECS Solid State Lett.*, 2012, **1**, Q57–Q60.
25 N. Janani, C. Deviannapoorani, L. Dhivya and R. Murugan, *RSC Adv.*, 2014, **4**, 51228–51238.
26 J. S. Chappell, T. A. Ring and J. D. Birchall, *J. Appl. Phys.*, 1986, **60**, 383.
27 R. L. Coble, *J. Appl. Phys.*, 1961, **32**, 787.

28 J. Hojo, R. Oono and A. Kato, *J. Mater. Sci.*, 1980, **15**, 2335–2344.
29 E. Ino, *J. Soc. Mater. Sci.*, 1976, **25**, 1165–1168.
30 J. D. MacKenzie, M. E. Smith, P. Angerer and Y. Kameshima, *Thermochim. Acta*, 2000, **359**, 87–94.
31 D. A. C. Manning, E. I. C. Rae and J. S. Small, *Mineral. Mag.*, 1991, **55**, 183–195.
32 W. Xia, B. Xu, H. Duan, Y. Guo, H. Kang, H. Li and H. Liu, *ACS Appl. Mater. Interfaces*, 2016, **8**, 5335–5342.
33 Y. H. Zhang, F. Chen, R. Tu, Q. Shen and L. M. Zhang, *Key Eng. Mater.*, 2014, **616**, 217–222.
34 A. A. Hubaud, D. J. Schroeder, B. Key, B. J. Ingram, F. Dogan and J. T. Vaughey, *J. Mater. Chem. A*, 2013, **1**, 8813.
35 R. J. Chen, M. Huang, W. Z. Huang, Y. Shen, Y. H. Lin and C. W. Nan, *Solid State Ionics*, 2014, **265**, 7–12.
36 F. Tietz, T. Wegener, M. T. Gerhards, M. Giarola and G. Mariotto, *Solid State Ionics*, 2013, **230**, 77–82.
37 A. Orera, G. Larraz, J. A. R. Velamazan, J. Campo and M. L. Sanjuan, *Inorg. Chem.*, 2016, **55**, 1324–1332.
38 A. K. Jonscher, *Nature*, 1977, **267**, 673–679.
39 J. Sakamoto, E. Rangasamy, H. Kim, Y. Kim and J. Wolfenstine, *Nanotechnology*, 2013, **24**, 424005.
40 Y. Shimonishi, A. Toda, T. Zhang, A. Hirano, N. Imanishi, O. Yamamoto and Y. Takeda, *Solid State Ionics*, 2011, **183**, 48–53.
41 S. Afyon, F. Krumeich and J. L. M. Rupp, *J. Mater. Chem. A*, 2015, **3**, 18636–18648.
42 G. M. C. C. W. Ban, *Solid State Ionics*, 2001, **140**, 285–292.
43 K. Liu and C.-A. Wang, *Electrochem. Commun.*, 2014, **48**, 147–150.
44 S. Kumazaki, Y. Iriyama, K.-H. Kim, R. Murugan, K. Tanabe, K. Yamamoto, T. Hirayama and Z. Ogumi, *Electrochem. Commun.*, 2011, **13**, 509–512.
45 P. Jeevan Kumar, K. Jayanth Babu and O. M. Hussain, *Mater. Chem. Phys.*, 2014, **143**, 536–544.
46 C. M. Julien, K. Zaghib and H. Groult, *Inorganics*, 2014, **2**, 132–154.
47 P. Jeevan Kumar, K. Jayanth Babu, O. M. Hussain and C. M. Julien, *Ionics*, 2012, **19**, 421–428.
48 T. Kato, T. Hamanaka, K. Yamamoto, T. Hirayama, F. Sagane, M. Motoyama and Y. Iriyama, *J. Power Sources*, 2014, **260**, 292–298.
49 P. Jeevan Kumar, K. Jayanth Babu, O. M. Hussain and C. M. Julien, *Ionics*, 2012, **19**, 421–428.